

Tsunami Probability in the Caribbean Region

TOM PARSONS¹ and ERIC L. GEIST¹

Abstract—We calculated tsunami runup probability (in excess of 0.5 m) at coastal sites throughout the Caribbean region. We applied a Poissonian probability model because of the variety of uncorrelated tsunami sources in the region. Coastlines were discretized into 20 km by 20 km cells, and the mean tsunami runup rate was determined for each cell. The remarkable ~500-year empirical record compiled by O’LOUGHLIN and LANDER (2003) was used to calculate an empirical tsunami probability map, the first of three constructed for this study. However, it is unclear whether the 500-year record is complete, so we conducted a seismic moment-balance exercise using a finite-element model of the Caribbean-North American plate boundaries and the earthquake catalog, and found that moment could be balanced if the seismic coupling coefficient is $c = 0.32$. Modeled moment release was therefore used to generate synthetic earthquake sequences to calculate 50 tsunami runup scenarios for 500-year periods. We made a second probability map from numerically-calculated runup rates in each cell. Differences between the first two probability maps based on empirical and numerical-modeled rates suggest that each captured different aspects of tsunami generation; the empirical model may be deficient in primary plate-boundary events, whereas numerical model rates lack backarc fault and landslide sources. We thus prepared a third probability map using Bayesian likelihood functions derived from the empirical and numerical rate models and their attendant uncertainty to weight a range of rates at each 20 km by 20 km coastal cell. Our best-estimate map gives a range of 30-year runup probability from 0–30% regionally.

Key words: Tsunami, Caribbean, hazard, earthquake.

1. Introduction

On Sunday, August 4, 1946, a $M = 8.1$ earthquake struck off the northeastern shore of the Dominican Republic that caused extensive damage and loss of life. Luis Miura, a United Press correspondent, described the subsequent tsunami at Ciudad Trujillo: “With a swelling roar it rolled up the bay and smashed against the towns. Dwellings and shops were swept away by the waves. Slabs of walls and roofs were hurled inland from the shore.” The tsunami is thought to have killed 1790 people at Matancitas who went to collect fish from the exposed shore when the sea receded after the earthquake; the water returned as a 2.4 m wave that encroached nearly 1 km inland (O’LOUGHLIN and LANDER, 2003). Significant runups were recorded at Puerto Rico as well as many other sites on Hispaniola; in this paper we define significant tsunami runup to be in excess of 0.5 m. At least 10 significant tsunamis have been documented in the northern Caribbean since 1498,

¹ U.S. Geological Survey, Menlo Park, CA, U.S.A.

six of which are known to have resulted in loss of life. Previous tsunamis destroyed Port Royal, Jamaica, killing an estimated 2000 people in 1692, killed at least 10 Jamaicans on the island's south coast in 1780, and damaged the north coast of Hispaniola and the Virgin Islands in 1842. Population increases mean that now, 35.5 million people in the northern Caribbean region are at risk from tsunami inundation (GRINDLAY *et al.*, 2005).

In this paper we attempt to map out spatial variations in the probability of hazardous Caribbean tsunamis by using the lengthy historic record in combination with numerical modeling techniques. We first calculate purely empirical probabilities using the observed record. We then investigate whether the ~ 500 -yr historical record is likely to be complete by comparing the observed and expected regional seismic moment as calculated with a finite-element model of Caribbean plate subduction. We then use the modeled slip-rate distribution in combination with tsunami generation and hydrodynamic models for individual earthquakes to calculate multiple synthetic tsunami catalogs. We lastly produce a probability map of the region where tsunami probabilities calculated from the long-term synthetic catalog are combined with the empirical model using a Bayesian method.

2. Historical Tsunami Catalog

2.1. Empirical Runup Frequencies

A motivating factor in making a probabilistic tsunami hazard assessment for the Caribbean region is the remarkable written record that has its first observation dating back to 1498. We identify 116 individual observations of tsunami runups in excess of 0.5 m in Table 1 that were used to establish empirical estimates of Caribbean tsunami frequency. To calculate empirical tsunami frequency, we gridded the Caribbean region into 20 km by 20 km cells, and summed the number of runup observations (≥ 0.5 m) in each cell (Fig. 1). The rate within a cell is simply the number of observed events divided by the total observation time. We use the total catalog duration for observation time so that the open intervals can be included.

The empirical tsunami record shows evidence for highest activity in the northern Caribbean region, especially the islands of Hispaniola, Puerto Rico, and the Virgin Islands in the Greater Antilles, and the northern end of the Lesser Antilles along the Caribbean subduction zone (Fig. 1). There is little to no record for much of Cuba and the South American coastline west of Venezuela having been affected in the past 500 yrs, which could be a reporting issue. Although, this pattern of tsunami activity is mirrored by the distribution of large earthquakes (Fig. 2), which would likely be felt regionally.

A key question is to what extent the observed spatial distribution of runups is related to the distribution of earthquake sources vs. areas that might be sheltered from high-amplitude tsunamis by benefit of location (areas protected by other islands that lie in principal propagation paths for example). A further important question regarding the empirical catalog is whether 500 years is long enough to represent the full hazard. For

Table 1

Database of Caribbean tsunami observations with runup ≥ 0.5 m sources: (NOAA online database; O'LOUGHLIN and LANDER, 2003). Runup values are estimates in most cases. Inundation refers to maximum approximate distance water was observed inland from tidal zone.

<u>Tsunami Source</u>					<u>Runup Location</u>		<u>Runup Measurements</u>	
Year	Mo.	Day	Country	Name	Lat.	Lon.	Max water height (m)	Max inundation (m)
1530	9	1	Venezuela	Cumana	10.483	-64.2	6	-
1530	9	1	Venezuela	Isla Cubagua	10.817	-64.183	6	-
1530	9	1	Venezuela	Paria	10.627	-62.167	7.3	-
1692	6	7	Jamaica	Port Royal	17.917	-76.867	1.8	-
1755	11	1	Antigua and Barbuda	Antigua Island	17.12	-61.78	3.7	-
1755	11	1	Barbados	Carlisle Bay	13.083	-59.617	1.5	-
1755	11	1	Cuba	Santiago de Cuba	20	-75.817	-	-
1755	11	1	Dominica	Portsmouth	15.567	-61.45	3.7	-
1755	11	1	Dominican republic	Samana Bay	19.217	-69.317	3.7	-
1755	11	1	Martinique	Martinique	14.667	-61	1.8	-
1755	11	1	Netherlands Antilles	Saba Island	17.633	-63.1	7.6	-
1755	11	1	Saint Martin	Saint Martin Harbor	18.083	-63.083	4.5	-
1755	11	1	Saint Vincent	Lesser Antilles	12	-62	4.5	-
1755	11	18	Saint Martin	Saint Martin Harbor	18.083	-63.083	-	-
1761	3	31	Barbados	Barbados	13.167	-59.533	1.2	-
1780	10	3	Jamaica	Savanna la Mar	18.217	-78.133	3.2	-
1798	2	22	Costa Rica	Barra de Matina	10.005	83.055	0.5	-
1822	5	7	Costa Rica	Barra de Matina	10.005	83.055	0.5	-
1842	5	7	Dominican Republic	Santo Domingo	18.47	-69.95	2	-
1842	5	7	Haiti	(north coast)	19.8	-70.683	2	-
1842	5	7	Haiti	Ile de la Tortue	20.04	-72.75	2	-
1842	5	7	Haiti	Port-de-Paix	19.933	-72.867	4.6	-
1842	5	7	USA Territory	Saint John	17.766	-64.748	3.1	-
1843	2	8	Antigua and Barbuda	Antigua	17.12	-61.85	1.2	-
1853	7	15	Venezuela	Puerto Sucre	10.464	-64.194	5	-
1856	8	9	Honduras	Omoa	15.75	-88.167	5	-
1867	11	18	Antigua and Barbuda	Antigua: St. Johns	17.193	-62.416	2.4	-
1867	11	18	Antigua and Barbuda	West coast	17.717	-61.817	1.4	-
1867	11	18	British Virgin Islands	Peter's Island	18.367	-64.633	1.2	-
1867	11	18	British Virgin Islands	Road Town	18.414	-64.616	1.5	9
1867	11	18	Dominica	Rupert's Bay	15.5	-61.333	3	-
1867	11	18	Grenada	Charlotte Town	12.167	-61.733	3	-
1867	11	18	Grenada	Saint George's	12.015	-61.778	1.5	-
1867	11	18	Guadeloupe	Basse Terre	16	-61.717	1	-
1867	11	18	Guadeloupe	Deshaies	16.317	-61.783	10	-
1867	11	18	Guadeloupe	I'les des Saintes	15.867	-61.617	1	-
1867	11	18	Guadeloupe	Sainte-Rose	16.333	-61.7	10	-
1867	11	18	Saint Lucia	Layon	13.883	-60.967	0.9	-
1867	11	18	Saint Vincent	Bequia island	13.28	-61.25	1.8	146
1867	11	18	St. Thomas	Charlotte Amalie	18.367	-64.933	2.4-4.3	-

Table 1

contd.

<u>Tsunami Source</u>					<u>Runup Location</u>		<u>Runup Measurements</u>	
Year	Mo.	Day	Country	Name	Lat.	Lon.	Max water height (m)	Max inundation (m)
1867	11	18	St. Thomas	St. Thomas Harbor	18.367	-64.933	9.1-18.3	-
1867	11	18	St. Thomas	West Gregerie Channel	18.328	-64.955	9	-
1867	11	18	St. Thomas	Little Saba	18.341	-64.982	12	-
1867	11	18	St. Thomas	Water Island	18.323	-64.952	7	-
1867	11	18	St. Thomas	Hassel Island	18.3	-64.96	4.9	-
1867	11	18	St. Thomas	Prince Rupert's Ledge	18.33	-64.926	7	-
1867	11	18	St. Croix	Christiansted and Frederiksted	17.756	-64.799	7.6-9	-
1867	11	18	USA Territory	Puerto Rico: Arroyo	17.983	-66.05	6.1	40
1867	11	18	USA Territory	Puerto Rico: Bahia de San Juan	18.45	-66.117	0.9	-
1867	11	18	USA Territory	Puerto Rico: Fajardo	18.34	65.66	6.1	-
1867	11	18	USA Territory	Puerto Rico: Salinas	17.975	-66.29	6.1	-
1867	11	18	USA Territory	Puerto Rico: Vieques	18.15	-65.45	6.1	-
1867	11	18	USA Territory	Puerto Rico: Culebra	18.305	-65.3	6.1	-
1867	11	18	USA Territory	Puerto Rico: Yabucoa	18.033	-65.883	1.37	-
1867	11	18	USA Territory	Charlotte Amalie	18.367	-64.933	6	-
1867	11	18	USA Territory	Frederiksted	17.717	-64.883	7.6	76
1867	11	18	USA Territory	Hassel Island	18.3	-64.96	4.9	-
1867	11	18	USA Territory	Saint Croix	17.75	-64.75	7	-
1868	3	17	Saint Vincent	Bequia Island	13	-61.25	0.9	21
1868	3	17	USA Territory	Puerto Rico: Arroyo	17.983	-66.05	1.5	-
1868	3	17	USA Territory	Charlotte Amalie	18.367	-64.933	0.6	-
1882	9	7	Panama	San Blas Archipelago	9.533	-78.917	3	-
1900	10	29	Venezuela	Puerto Tuy	10.333	-65.917	10	-
1902	8	30	Martinique	Fort de France	14.6	-61.083	1	-
1906	1	31	Panama	Naos Is.	8.917	-79.533	0.7	-
1907	1	14	Jamaica	Annotto Bay	18.267	-76.767	2.2	9
1907	1	14	Jamaica	Buff Bay	18.233	-76.667	2.5	-
1907	1	14	Jamaica	Hope Bay	18.2	-76.567	2.5	-
1907	1	14	Jamaica	Kingston Harbor	17.967	-76.8	2.5	-
1907	1	14	Jamaica	Ocho Rios	18.4	-77.1	2.5	-
1907	1	14	Jamaica	Orange Bay	18.367	-78.317	2.5	-
1907	1	14	Jamaica	Port Antonio	18.167	-76.45	2.5	-
1907	1	14	Jamaica	Port Maria	18.367	-76.9	2.4	-
1907	1	14	Jamaica	Saint Ann's Bay	18.433	-77.2	2.5	-
1907	1	14	Jamaica	Sheerness Bay	18.317	-76.8	2.5	-
1916	4	25	Panama	Isla Col-n	9.385	-82.265	0.5	-
1916	4	25	Panama	Bocas del Toro	9.333	-82.55	0.6	-
1916	4	25	Panama	Careening Cay	9.333	-81.75	1.3	-
1918	10	11	British Virgin Islands	Tortola Island	18.667	-64.65	0.7	-
1918	10	11	Dominican Republic	Rio Ozama	18.47	-69.95	0.7	-

Table 1

contd.

<u>Tsunami Source</u>					<u>Runup Location</u>		<u>Runup Measurements</u>	
Year	Mo.	Day	Country	Name	Lat.	Lon.	Max water height (m)	Max inundation (m)
1918	10	11	USA Territory	Puerto Rico: Aguadilla	18.45	-67.133	3.7	-
1918	10	11	USA Territory	Puerto Rico: Arecibo	18.448	-66.733	0.6	-
1918	10	11	USA Territory	Puerto Rico: Bahia de Boqueron	18.463	-66.084	1.1	-
1918	10	11	USA Territory	Puerto Rico: Caja de Muertos	17.867	-66.533	1.5	15
1918	10	11	USA Territory	Puerto Rico: Cayo Cardona	17.959	-66.365	0.75	-
1918	10	11	USA Territory	Puerto Rico: Guanica	17.983	-66.917	0.5	-
1918	10	11	USA Territory	Puerto Rico: Isabela	18.5	-67.033	2	-
1918	10	11	USA Territory	Puerto Rico: Isla Mona	18.08	-67.9	4	-
1918	10	11	USA Territory	Puerto Rico: Mayaguez	18.217	-67.15	1.5	-
1918	10	11	USA Territory	Puerto Rico: Punta Agujereada	18.51	-67.167	6.1	-
1918	10	11	USA Territory	Puerto Rico: Punta Borinquen	18.484	-67.169	4.5	100
1918	10	11	USA Territory	Puerto Rico: Punta Higuero	18.367	-67.267	5.5	-
1918	10	11	USA Territory	Puerto Rico: Rio Culebrinas	18.4	-67.183	4	-
1918	10	11	USA Territory	Puerto Rico: Rio Grande de Loiza	18.45	-65.883	1	-
1918	10	11	USA Territory	Saint Thomas: Krum Bay	18.329	-64.961	1.2	-
1931	10	1	Cuba	Playa Panchita	22.95	-80.417	1	-
1946	8	4	Dominican Republic	Northern coast	19.7	-70.5	4.6	-
1946	8	4	Dominican Republic	Nagua	19.417	-69.817	5	-
1946	8	4	Dominican Republic	Rio Boba	19.467	-69.867	5	-
1946	8	4	USA Territory	Puerto Rico: San Juan	18.483	-66.133	0.66	-
1946	8	8	USA Territory	Puerto Rico: San Juan	18.483	-66.133	0.6	-
1953	5	31	Dominican Republic	Puerto Plata	19.8	-70.683	0.06	-
1969	12	25	Barbados	Barbados	13.167	-59.533	0.46	-
1976	2	4	Honduras	Puerto Cortes	15.833	-87.917	0.45	-
1969	12	25	Dominica	Dominica	15.5	-61.3	0.12	-
1985	3	16	Guadeloupe	Basse Terre	16	-61.717	0.12	-
1989	11	1	USA Territory	Puerto Rico: Cabo Rojo	18.083	-67.15	0.1	-
1991	4	22	Costa Rica	R'o Mo'n	9.73	-82.84	3	-
1991	4	22	Costa Rica	Puerto Viejo	10.5	-83.5	2	-
1991	4	22	Panama	Coco Solo	9.37	-79.881	0.76	-
1991	4	22	Panama	Isla de Carenero	9.33	-82.33	2-3	-
1991	4	22	Panama	Portobelo	9.55	-79.617	0.6	-
1997	12	26	Montserrat	Old Road Bay	16.737	-62.236	3	80

Table 1

contd.

<u>Tsunami Source</u>					<u>Runup Location</u>		<u>Runup Measurements</u>	
Year	Mo.	Day	Country	Name	Lat.	Lon.	Max water height (m)	Max inundation (m)
2003	7	12	Guadeloupe	Deshaies	16.317	-61.783	1	25
2003	7	12	Guadeloupe	Vieux Habitants	16.05	-61.75	0.6	-
2003	7	12	Montserrat	Farm Bay	16.737	-67.153	4	-

example, it is evident that the southern part of the Caribbean subduction zone in the Lesser Antilles has produced fewer earthquakes and tsunamis during the past 500 years than has the northern part (Figs. 1, 2). This might reflect genuine differences in the seismic production of the zone, or the southern part of the subduction zone might represent a seismic gap waiting to be filled. We address these issues in detail in Sections 4 and 5. In the next section, we pursue calculation of empirical tsunami probabilities under the assumption that the catalog observations are complete and representative.

3. Monte Carlo Estimation of Rate-Model Uncertainty

Tsunamis affect broad areas as they propagate away from their sources, and a region as complex as the Caribbean has widely distributed tsunamigenic sources. Since tsunamis resulting from multiple seismic sources operating at different recurrence intervals can affect a given coast, the best probability model is one that is time-independent, such as a Poisson process built around an exponential distribution (e.g., GEIST and PARSONS, 2006; 2008). We thus used observed tsunami runups to calculate rate parameters (λ) in the exponential probability density distribution as

$$f(t) = \lambda e^{-\lambda t}, \quad \text{for } t > 0, \quad (1)$$

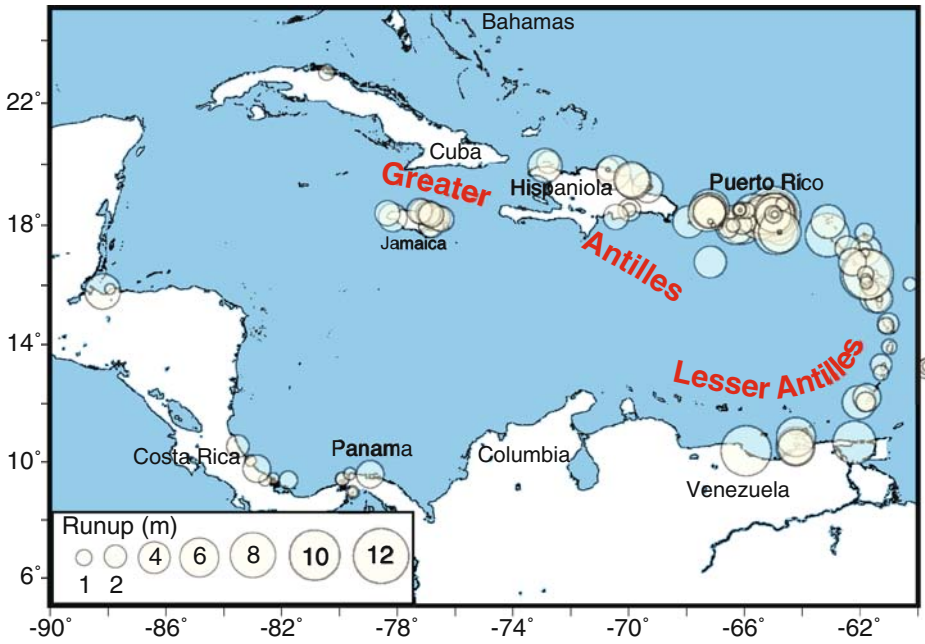
which when integrated over a given duration gives a time-independent cumulative probability.

Estimation of the event rate λ (inverse of the recurrence interval) for a small number of observations is subject to considerable uncertainty. Further, since the observation period begins at an arbitrary time, and we have no knowledge of what happened before 1498, we wish to treat the first open interval properly. To accomplish both objectives, we rely on Monte Carlo modeling of the tsunami runup frequencies (PARSONS, 2008).

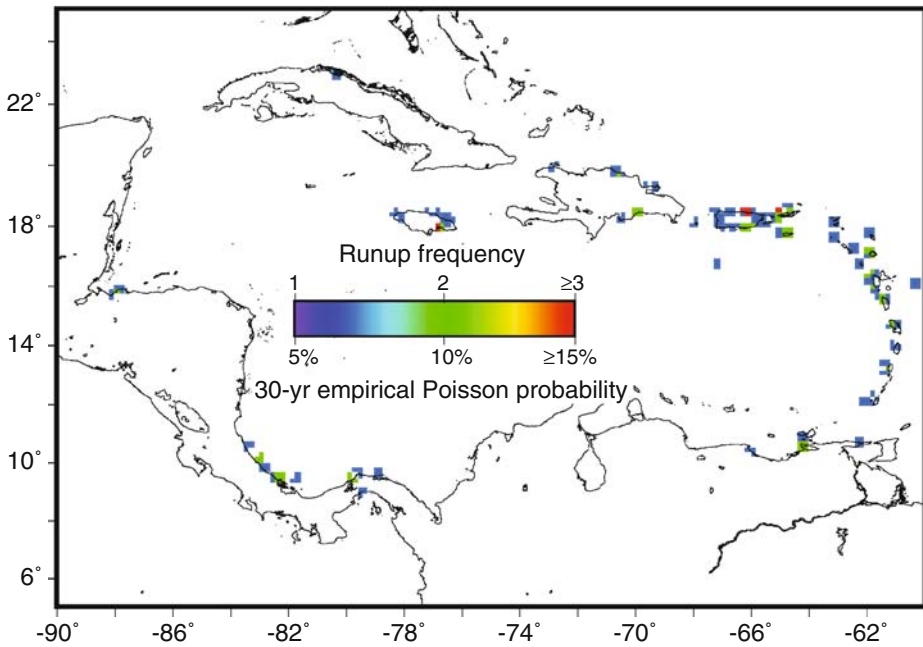
Figure 1

Top shows individual runup observations as noted in Table 1. Circle size represents runup in m. Bottom panel shows summed number of runup observations per 20 km by 20 km cell and the corresponding empirical Poisson probability. ▶

Tsunami runup observations



Tsunami frequency in 20 km by 20 km cell



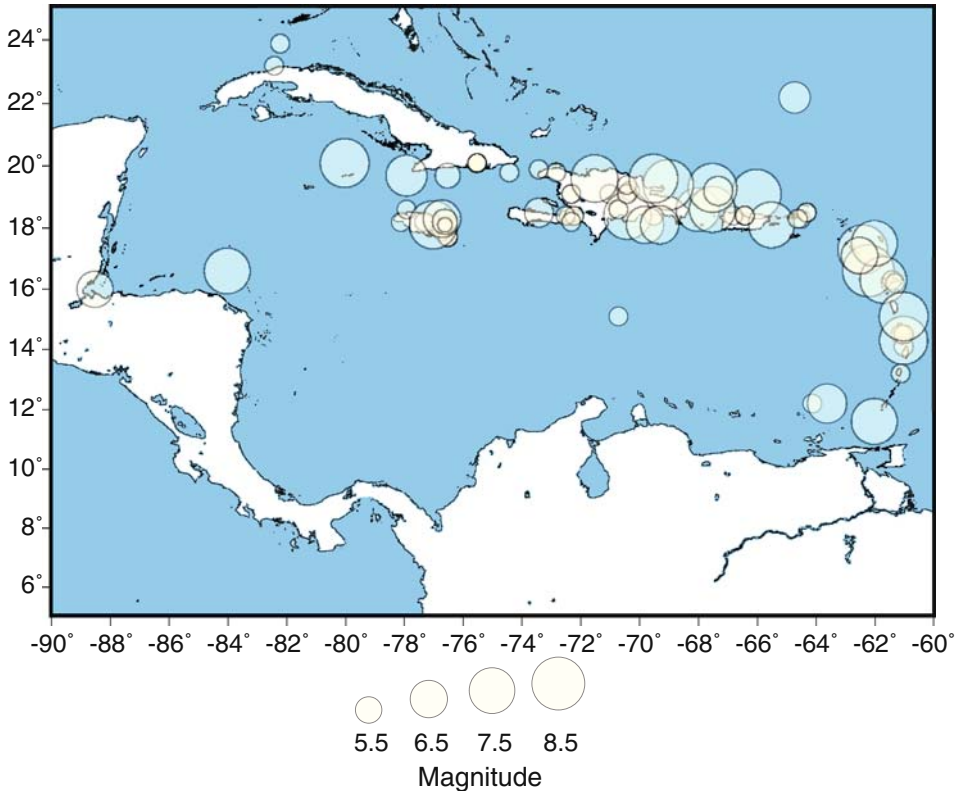


Figure 2

500-yr catalog of large ($M \geq 5$) earthquakes in the Caribbean region. Locations of older events are approximations based on historical accounts. The completeness threshold varies with time, and is likely $\sim M = 7$ before the 20th century. Sources: SHEPHERD, 1993; NEIC, Significant Worldwide Earthquakes (NOAA).

Here it is assumed that if an exponential distribution is used to calculate tsunami probability, then the best way to estimate the range of possible rate parameters that fit the observations is to find those that most commonly reproduce observed tsunami frequencies. The first step was construction of a series of distributions that covered all reasonable rates ($1/10$ to $1/3000 \text{ yrs}^{-1}$). Rates were randomly drawn 100,000 times from each series and assembled into tsunami event sequences. These Monte Carlo sequences began with events given freedom to happen any time before 1498. The extra events were not counted into the frequencies, but did establish starting points for Monte Carlo sequences. This was needed because it is expected that tsunamis occurred prior to 1498, but we have no knowledge of them other than that. In this way we avoided the arbitrary starting time having undue influence on rate estimation.

Each event sequence that matched the observed frequencies was tallied. A distribution of matches to the observed record was produced (Fig. 3), and the mode

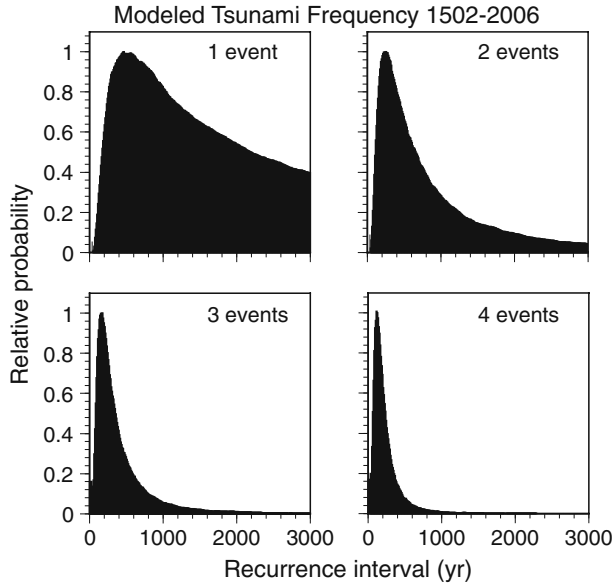


Figure 3

Normalized histograms of the Monte Carlo sequences that matched the indicated event frequencies over 500-year intervals. Ranges of exponential rate parameters are shown (expressed as the inverse, which is recurrence interval) that can match observed frequencies of Caribbean tsunami runups (≥ 0.5 m), which range from 1 to 4 events in ~ 500 yrs.

(most frequent value), median, or mean of that distribution can be taken to represent the rate parameter. This approach also simultaneously estimates uncertainty in the rate parameter resulting from small sampling, and the influence of the open intervals. The Monte Carlo techniques we used are discussed in detail by PARSONS (2008) in relation to paleoseismic earthquake observations.

4. Poisson Probability of Tsunami Occurrence from Empirical Analysis

In the Poisson model, probability depends on the rate parameter (discussed in Section 2) and the duration (Δt) of the interval of interest. Probability is given by

$$P(\Delta t) = 1 - e^{-\lambda \Delta t}. \quad (2)$$

Probability calculation from the rates shown in Figure 3 then is straightforward using Equation (2). Results are shown in Figures 1 and 4. As can be seen from Figure 4, there is considerable spread in probability that results from the spread of possible rates (Fig. 3) consistent with the observed number of runups ≥ 0.5 m in the 20 km by 20 km cells. Mean 30-year probability for sites with one event over the observation period is 4%, for cells with two events the mean is 7%, for three events the mean is 12%, and for four

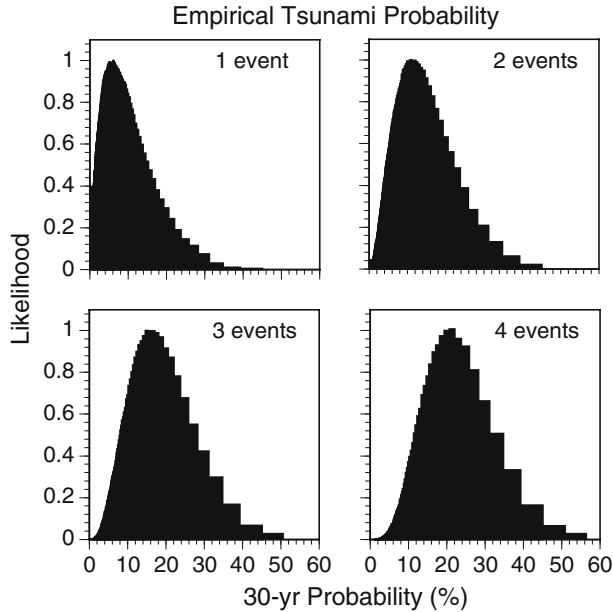


Figure 4

Normalized histograms indicating the likelihood of a given 30-yr Poisson probability resulting from the rate parameters shown in Figure 3, for 20 km by 20 km cells with observations of 1 to 4 events in ~ 500 yrs. Means and confidence intervals are given in Table 2.

events the mean is 17%. Using empirical rates under a time-independent Poisson model thus causes the hazard estimate to be greatest where runups were most frequently observed in the past, and assumes that future events will most likely happen where past ones have. In contrast, a time-dependent, renewal, or seismic gap model might place the greatest hazard near submerged faults where little activity has been observed in the recent past.

Given the wide range of credible probability results shown in Figure 4, it is difficult to know what single value might best represent tsunami hazard. The mean value is an obvious choice, although the distributions of possible probability values are not symmetrical (e.g., Gaussian). Thus it is perhaps more useful to think of the hazard in terms of confidence bounds. For example if the empirical model is assumed to be valid, then we can state with 95% confidence that a site that experienced four tsunamis with runup in excess of 0.5 m since 1498 has a 3% to 42% probability of another such event in the next 30 yrs (Table 2).

A central question surrounding exclusive use of empirical tsunami runup rates for future hazard calculations is how complete the empirical record is, and how representative the past ~ 500 -yr-period has been. Examination of Table 1 shows a much higher frequency of observation in the 19th century as compared with the previous centuries, implying that increased population density increased the number of

Table 2

30-year probabilities of tsunami runup (≥ 0.5 m) in the 20 km by 20 km cells shown in Figure 1, which contain observations from 1 to 4 past events. 95% and 67% confidence intervals on the probability values as well as means (PARSONS, 2008) are given.

<i>30-Year Poisson probability from empirical rates</i>				
Confidence bound	1 Event	2 Events	3 Events	4 Events
97.5%	14%	23%	32%	42%
83.5%	6%	11%	18%	26%
Mean	4%	7%	12%	17%
16.5%	1%	2%	4%	8%
2.5%	1%	1%	2%	3%

observations. Additionally, since the Caribbean catalog is dominated by local-earthquake generated tsunamis, we want to know whether the 500-yr earthquake catalog has released all the expected seismic moment, or whether there needs to be more large earthquakes to satisfy a moment deficit. In the next section we discuss calculation of expected moment and comparison with the moment expressed in the seismic catalog.

5. Is the 500-year Tsunami Catalog Representative? Expected vs. Expressed Seismic Moment in the Caribbean Region

5.1. Model Development

To calculate the expected seismic moment rate in the Caribbean region, we developed a 3-D finite-element model of long-term fault slip (Fig. 5). The purpose was to displace the Caribbean plate relative to North America to simulate slip along the primary plate boundaries. The model tracked the amount of expected slip, which was used to calculate seismic moment accumulation, assuming all of the slip in the seismogenic zone is released during earthquakes. The results gave a sum of total moment that we used to compare with observed seismic moment, as well as a spatial distribution of expected moment. The nature of the problem made a 3-D approach necessary because: (1) Caribbean plate motion is rotational relative to North America, (2) the model involves permanent deformation because lithosphere is variably consumed along the subduction front, and (3) the calculated relative slip rates and rakes are used to generate synthetic tsunamigenic earthquake events.

The model consisted of two blocks that represented the lithosphere on either side of the Caribbean plate boundary with the North American plate. To define the plate boundary geometry, we used surface traces of the primary strike-slip boundary and subduction front (MANN *et al.*, 2007). We extended the strike-slip boundary on the northwestern edge of the Caribbean plate vertically through the crust. We defined the subduction-zone shape from

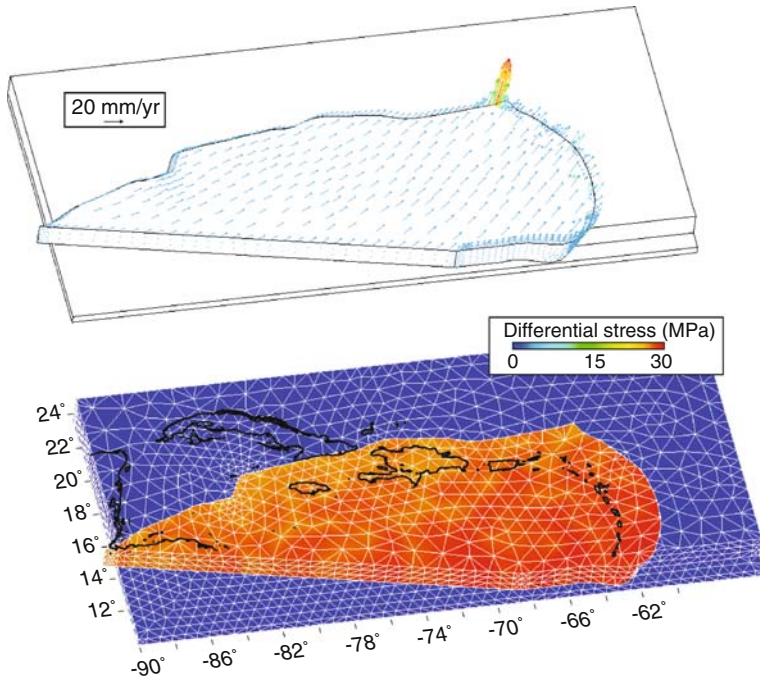


Figure 5

Finite-element model of the submerged parts of the Caribbean-North American plate boundaries. Strike-slip boundary to the northwest is vertical, while the subduction zone is variably dipping according to CRUCIANI *et al.* (2005). The top figure shows displacement vectors, and the color shading on the Caribbean plate below displays small variations in differential stress resulting from displacement.

the database of CRUCIANI *et al.* (2005), who used seismic tomography and earthquake hypocenters to constrain subducted slab geometries. We interpolated the transition from strike-slip into subduction smoothly as shown in Figures 5 and 6. The model Caribbean plate was displaced relative to the North American plate according to the Caribbean-North American “hybrid” rotation pole (latitude = 64.9°N, longitude = 250.5°E, $\omega = 0.214^\circ/\text{Myr}$) of DEMETS *et al.* (2000), based in part on GPS measurements reported by DIXON *et al.* (1998).

Volumes were meshed by first estimating element edge lengths for all defining lines. The element edge lengths on these lines were then refined for curvature and proximity of faults in the geometry. The mesh was thus finest where volumes changed shape the most, and in regions of greatest complexity. The model was composed of 24,509 elastic tetrahedral elements defined by 36,412 nodes with an average node spacing of 50 km. Elements were defined by 10 nodes, each having three degrees of freedom (translations in the nodal x, y, and z directions).

Our Caribbean finite-element model had two major contact zones, representing subduction of the North American plate beneath the Caribbean, and transition into strike-

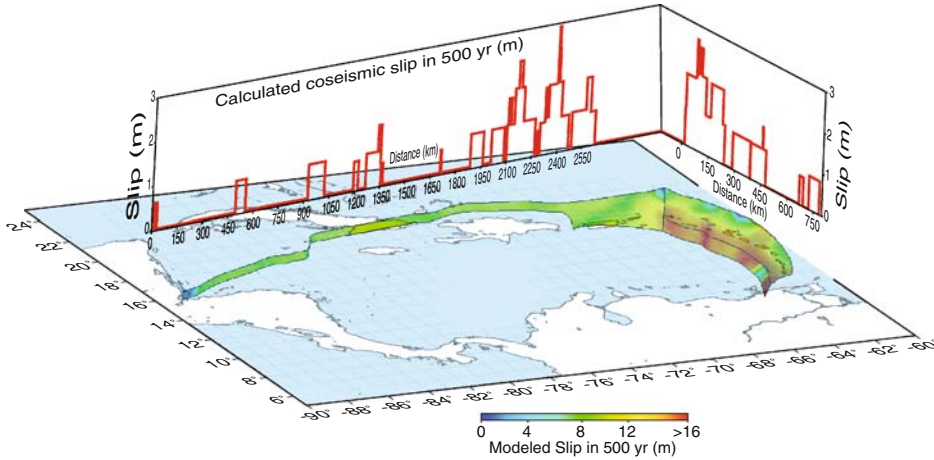


Figure 6

Distribution of slip rate on the submerged Caribbean plate boundary for a 500-yr simulation period (color shading). Approximate seismic slip compiled from the catalog in Figure 2 is shown for comparison (red graph). Slip was derived from reported magnitudes using regressions of WELLS and COPPERSMITH (1994).

slip motion along the northern Caribbean plate to the northwest (Fig. 5). These faults were deformable, and were constructed from contact elements obeying the Coulomb failure stress (CF) relation

$$CF \equiv \bar{\tau}_f + \mu\sigma_n, \tag{3}$$

where $\bar{\tau}_f$ is shear stress acting on a fault surface, μ is the friction coefficient, and σ_n is the component of stress acting normal to a fault surface. Contact elements had zero thickness and were welded to the sides of tetrahedral elements. We assigned a low friction coefficient ($\mu = 0.2$) to the subduction and strike-slip interfaces (e.g., CATTIN *et al.*, 1997; RUFF, 2002; KOPF and BROWN, 2003).

We loaded our model by decomposing the Caribbean plate rotation into E-W and N-S vectors at each model node within the Caribbean plate. These combined motions resulted in a $\sim 18\text{--}20$ mm/yr of relative plate motion depending on the plate-boundary orientation. The Caribbean block was constrained not to sink along its base, but could slip freely, simulating the asthenosphere-lithosphere boundary. Rather than subducting the North American plate beneath the Caribbean in the model, we caused the Caribbean plate to override North America, which generates the equivalent moment accumulation, but is a much simpler model because no subduction channel was required. We ran the model for a 10,000-year simulation to ensure steady-state slip along the plate boundaries and extracted 500-yr periods for comparison with observed seismic moment release. Total slip divided by 500 years gave the long-term slip rate distribution.

6. Comparison between Expected and Observed Seismic Moment

Our model of Caribbean-North American plate interaction enabled calculation of expected slip rate distribution (\dot{u}) on the interplate megathrust and strike-slip zones, which was used to calculate the tectonic moment rate (\dot{m}_t) distribution, as $\dot{m}_t = \mu A \dot{u}$, where A is fault area and μ is the shear modulus (where $\mu = 3 \cdot 10^{11}$ dyne-cm⁻²) (Fig. 6).

We calculated the total tectonic moment for a 505-year period (duration of seismic catalog AD1502-2006) to be $7.42 \cdot 10^{29}$ dyne-cm on the surface shown in Figure 6. The expressed seismic moment sum from the earthquake catalog shown in Figure 2 is $2.39 \cdot 10^{29}$ dyne-cm. Thus the ratio of expressed seismic to expected tectonic moment release (coupling coefficient) is $c = 0.32$. We note that KAGAN (2002a; 2002b) arrived at a similar low coupling coefficient for the Caribbean region using modern catalog data, and a simpler plate boundary model. One of two conclusions can be drawn from this result: (1) The seismic coupling coefficient around the Caribbean plate is low, or (2) there is a large temporal seismic gap waiting to be expressed.

If we were to accept the low seismic coupling estimate for the Caribbean region, then we could further conclude that the tsunami runup probabilities we calculated from the empirical rates represent a valid forecast. However, if the 500-yr observation period is deficient, then we require an alternative runup rate model. We pursue such a model in Section 7, where the slip rates derived from the finite-element model are discretized into earthquake events, some of which are tsunamigenic (i.e., result in ≥ 0.5 m runups). We then applied a hydrodynamic model to assess runup potential throughout the Caribbean region.

7. Numerical Models of Expected Tsunami Frequency

If we know the slip rate along the Caribbean plate boundaries, we can calculate the expected rate of earthquakes greater than a certain magnitude using a Gutenberg-Richter magnitude-frequency distribution. Some percentage of these events is expected to cause observable tsunamis. Tsunami runups for a given earthquake can be approximated using standard generation and hydrodynamic models; multiple realizations can give an estimate of the likely range in frequencies at any coastal location in the model (e.g., GEIST and PARSONS, 2006). Given the very real possibility that the past 500-yr observations are incomplete, we describe the development of an alternative tsunami rate model below, which is based on the modeled slip-rate distribution from Section 4 and the assumption of complete seismic coupling along the Caribbean plate boundary.

7.1. General Probabilistic Framework

To develop synthetic tsunami catalogs, we used a general aggregation equation for determining the rate (λ) at which tsunamis will exceed a certain runup (R_0) at a coastal location as

$$\lambda(R > R_0) = \sum_{\text{type}=i} \sum_{\text{zone}=j} v_{ij} \int P(R > R_0 | \psi_{ij}) f_{\psi}(\psi_{ij}) d\psi, \quad (4)$$

where the index i refers to the type of tsunami source (e.g., $i = 1$ earthquakes, $i = 2$ landslides, etc.), index j the zone which that source occurs in (according to some particular zonation scheme), v_{ij} the mean rate for source (i, j) , ψ_{ij} the tsunami source parameters for source (i, j) , f_{ψ} the probability distribution for tsunami source parameters, and $P(R > R_0 | \psi_{ij})$ is the probability that runup will exceed R_0 at the coastal location for a given source parameter (GEIST and PARSONS, 2006; GEIST *et al.*, 2008). For this study, we only considered earthquake-generated tsunamis scaled according to the seismic moment m , where moment magnitude M is related to seismic moment according to $M = (2/3)(\log m - 9.05)$ (HANKS and KANAMORI, 1979). Equation (4) therefore is reduced to

$$\lambda(R > R_0) = \sum_{\text{zone}=j} v_j \int_{m_t}^{\infty} P(R > R_0 | m_j) f_j(m) dm. \quad (5)$$

Propagation distance was included in the term $P(R > R_0 | m_j)$ since this term is computed by numerical propagation models described below. The term $f_j(m)$ is the frequency-moment distribution for earthquakes in zone j . We used the tapered Gutenberg-Richter (G-R) distribution in which the complementary cumulative (survivor) distribution $F_j(m)$ is given by (KAGAN, 2002a; KAGAN and JACKSON, 2000)

$$F_j(m) = (m_t/m)^{\beta} \exp\left(\frac{m_t - m}{m_c}\right), \quad m \geq m_t, \quad (6)$$

where β is the shape parameter for the distribution, m_t is the threshold moment, and m_c is the corner moment that controls the tail of the distribution.

7.2. Seismic Zonation

The northern boundary of the Caribbean plate was divided into 7 zones in which the rate calculations were aggregated. The first two zones represented the eastern and western parts of the Cayman transform fault, separated by the Cayman spreading center (LEROY *et al.*, 2000). The remaining zones represented the Greater Antilles (zones 3 through 5) and Lesser Antilles (zones 6 and 7) subduction zones. For each zone, the frequency-moment distribution parameters were set equal to the parameters determined from the global study of BIRD and KAGAN (2004) according to their tectonic setting: i.e., zones 1 and 2, $\beta = 0.64$ and $M_c = 8.14$ for slow oceanic transform faults and zones 3 through 7, $\beta = 0.64$ and $M_c = 9.58$ for subduction zones. See BIRD and KAGAN (2004) regarding uncertainty estimates associated with these values.

The source rate parameter for each zone (v_j) was defined as the activity rate for earthquakes of $m \geq m_t$ and is related to the seismic moment rate (\dot{m}_s) as described by KAGAN (2002b):

$$v(m) = \frac{(1 - \beta)\dot{m}_s}{m^\beta m_c^{1-\beta} \Gamma(2 - \beta) e^{m/m_c}}, \quad (7)$$

where Γ is the gamma function. The “tectonic” moment rate (\dot{m}_t) is given by $\dot{m}_t = \mu A \dot{u}$, where μ is the shear modulus, A is the area of the seismogenic part of the fault zone, and \dot{u} is the long-term slip rate along the fault determined from the finite-element modeling described in Section 5. \dot{m}_s and \dot{m}_t are related by a seismic coupling parameter ($0 \leq c \leq 1$): $\dot{m}_s = c \dot{m}_t$. For a fault that has no aseismic slip at seismogenic depths, $c = 1$. Since the empirical catalog already provides a low-coupling rate estimate, we assumed that $c = 1$ in determining the maximum activity rate of earthquakes for each zone from the tectonic rate.

To calculate \dot{m}_t for each zone, the long-term slip rate (\dot{u}) from the finite-element modeling was averaged over seismogenic depths. Fault lengths (L) were taken from the surface traces of the faults. For the oceanic transform faults, the fault width at seismogenic depths is taken from BIRD and KAGAN (2004), whereas for the subduction faults, the fault width was taken from ten BRINK and LIN (2004). A constant shear modulus of 30 GPa was assumed for each zone.

7.3. Monte Carlo Implementation

We implemented Equation (5) using a Monte Carlo-type procedure in which a synthetic earthquake catalog of fixed duration was prepared from random samples of the distribution defined by Equations (6) and (7). Two different Monte Carlo analyses were conducted: (1) Tsunami results were aggregated from 310 $M \geq 7$ earthquakes representing a single catalog of duration 4,442 years and (2) tsunami results were aggregated from 50 separate earthquake catalogs of duration 500 years each (approximately the duration of the observed earthquake catalog). The number of earthquakes sampled from the tapered G-R distribution (Equation (8)) varied for each source zone, depending on \dot{m}_t . For a given time period τ , the expected number of earthquakes of moment $m \geq m_t$ was derived from (7) (cf., McCaffrey, 1994):

$$N(m > m_t) = \frac{(1 - \beta)\dot{m}_t \tau}{m_t^\beta m_c^{1-\beta} \Gamma(2 - \beta) e^{m_t/m_c}}. \quad (8)$$

The location of each earthquake was randomly varied within each source zone according to a uniform distribution.

Other source parameters were scaled with respect to seismic moment according to global scaling relationships. For subduction zones, the fault length scaling relationship was taken from the LAY *et al.* (1982) catalog of subduction zone earthquake source

parameters, updated to include more recent earthquakes (GEIST, 2002). For the oceanic transform fault, the WELLS and COPPERSMITH (1994) scaling relationship was used. Fault width was assumed to be half the fault length (GELLER, 1976), with a maximum fault width constrained by the dimensions of the seismogenic zone. Each earthquake had a stochastic slip distribution that conformed to a k^{-2} slip spectrum (HERRERO and BERNARD, 1994; TSAI, 1997) with average slip scaled to seismic moment based on the global subduction zone earthquake catalog.

For each earthquake, vertical and horizontal coseismic seafloor displacements are the initial conditions for tsunami modeling (TANIOKA and SATAKE, 1996). We calculated these displacements using OKADA'S (1985) analytic functions that are applicable for an elastic half-space. A finite rise-time of 20 s was applied uniformly along the rupture zone, with no preferred rupture propagation direction. We modeled the propagation of the tsunami wavefield using a finite-difference approximation to the linear long-wave equations (AIDA, 1969; SATAKE, 2002). A 2-arc-minute bathymetric grid (SMITH and SANDWELL, 1997) was used with an 8 s time step that satisfied the Courant-Friedrichs-Lewy stability criterion for the Caribbean region. A reflection boundary condition was imposed at the 250 m isobath, whereas a radiation boundary condition was imposed along the open-ocean boundaries of the model (REID and BODINE, 1968). Runup (R_0) was approximated from the coarse grid model for use in Equation (4) by finding the nearest model grid point to the coastline and then multiplying the peak offshore tsunami amplitude by a factor of 3 that roughly accounts for shoaling amplification and the runup process itself (SATAKE, 1995, 2002; SHUTO, 1991). For the first experiment (single 4,442-year synthetic catalog), the exceedance probability was calculated for 3 runup threshold values: 0.5 m, 1.0 m, and 2.0 m (Fig. 7). For the second experiment (fifty 500-year catalogs), the exceedance probability was calculated using a 0.5 m runup threshold for each of the 50 synthetic catalogs.

It is likely that runup varies considerably within the scale of our cell size. Significant focusing of tsunami waves from nearshore bathymetric variation can greatly amplify tsunami runup as exemplified in high resolution runup models (e.g., TITOV and SYNOLAKIS, 1997; MATSUYAMA *et al.*, 1999), such that the runup thresholds we use in our coarse-grid model are low-estimate values. Furthermore, in coastal low-lying regions, inundation from low runup regions can cover a large area, as exemplified by the 1 km inundation distance from the 2.5 m runup at Matanzas, Dominican Republic, in 1946.

We found that the fifty 500-year catalogs captured more variability in spatial runup distribution than did the 4442-year catalog. This resulted from the multiple catalogs having more variety of earthquake locations since a few very large events can dominate the distribution of moment, and consequently regional tsunami runup distribution, due to the Gutenberg-Richter constraint. We thus used the set of fifty 500-year catalogs to determine mean rates and uncertainties in the probability calculations that follow.

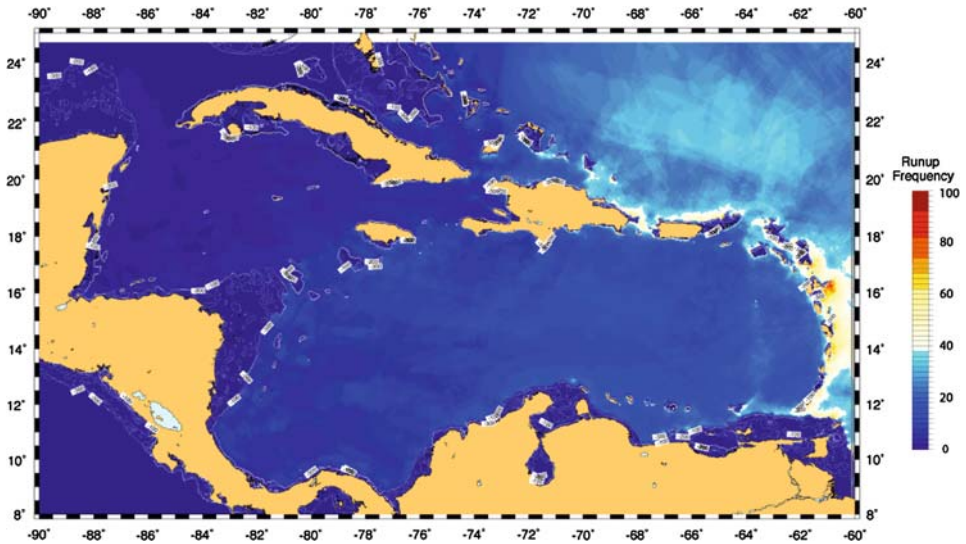


Figure 7

Example calculation of expected runup (≥ 0.5 m) frequency over a 4442-yr period calculated from the expected seismic moment rate shown in Figure 6.

8. Poisson Probability of Tsunami Occurrence from Numerical Modeling

8.1. Probability Mapping

Numerical models of expected tsunami frequency gave us an alternative estimate of the rate of $R_0 \geq 0.5$ -m runup throughout the Caribbean region (Fig. 7). We calculated Poisson probabilities from these rates in the same manner as was used for the empirical observations, and the results are shown in Figure 8. We used the mean frequency in Equation (2) at each 20 km by 20 km coastal cell from the 50 Monte Carlo runs described in Section 7.

Results from mapping probability from modeled tsunami rates show highest probability (~ 20 – 30% in 30 years) along the Lesser Antilles. The Greater Antilles also show significant runup probability in the 10–20% range, particularly in Puerto Rico and eastern Hispaniola. The majority of sites around the Caribbean region show low probability, which is evident in Figure 8. The overall distribution of values shows that the vast majority of 20 km by 20 km cells have 0–5% probability in 30 years (Fig. 9).

One concern with the probability results from the numerical model is that we used a simplified version of the plate boundary, which might have the effect of maximizing hazard along the subduction front, and omitting events emanating from accommodating intra-plate faults, particularly in the intra- and backarc regions of the Greater Antilles and the convergence zone north of Panama and South America (e.g., AUDEMARD and AUDEMARD, 2002), that were not in our model. In Section 10, we investigate ways of

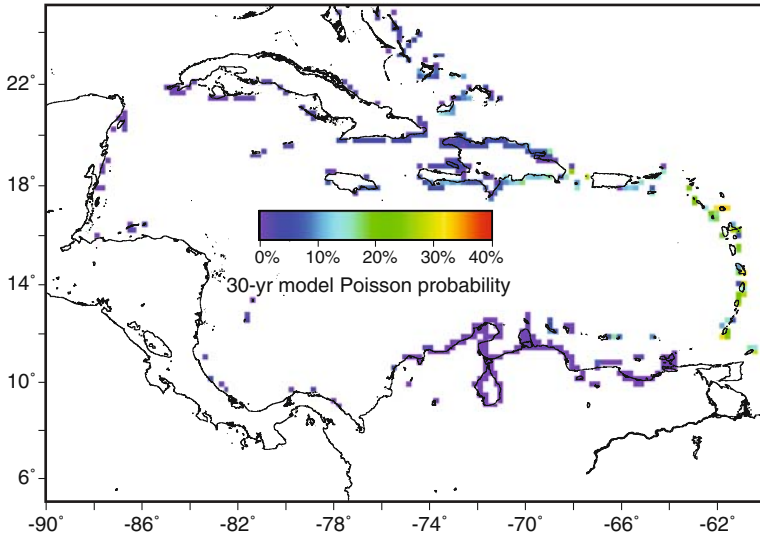


Figure 8

Mapping of 30-year Poisson probability calculations made from numerical modeling of tsunami runup rates.

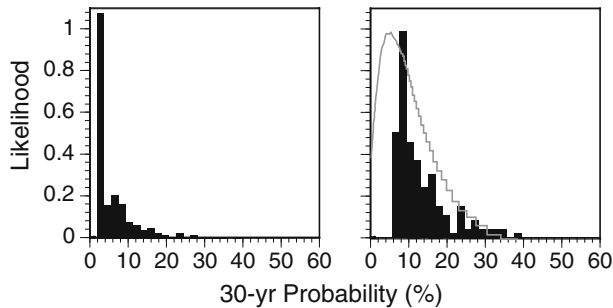


Figure 9

Histograms of 30-year runup (≥ 0.5 m) probability for all Caribbean coastlines modeled. The left panel shows results mapped in Figure 8; the vast majority of 20 km by 20 km cells have less than 5% probability. The right panel shows the distribution of values greater than 5%. The gray line gives an example shape from the empirical tsunami probability distributions shown in Figure 4 for comparison.

combining the numerically modeled rates with the empirical rates to account for the sources not included in the numerical models, but first we compare results from the two methods below.

9. Comparison of Empirically-Derived Probability with Model-Derived Values

One of the key reasons for undertaking the numerical modeling exercise for tsunami runup frequency was to determine if there were low-probability events associated with

plate boundary earthquakes not present in the empirical record, and if the spatial frequency patterns were similar, or greatly different. The probability map shown in Figure 8 indicates many regions with low probability that were not evident in the empirical mapping shown in Figure 1, including the coasts of Venezuela, Columbia, Cuba, and the Bahamas. These regions show 30-year probabilities of less than 5%, which loosely translates into rates fewer than 1 in 500 years, which may explain why the empirical map has virtually no observations from these regions (Fig. 1). These regions where the numerical-modeling results augment the empirical are straightforward to combine in an overall mapping, since there is no overlap. Where the two methods overlap and potentially conflict will require a relative weighting process for combination.

To assess similarities and differences between the empirical and numerically modeled results, we made two maps with the same probability thresholds (5–15%; Fig. 10). Perhaps the most obvious difference between the two models where they have overlapping results is along the Lesser Antilles, where modeled probabilities are nearly uniformly higher than empirical. This is a result of the numerical model having 100% seismic coupling vs. the observed seismic release being $\sim 30\%$ of the expected moment release. The model-derived probabilities are also higher than empirical along southern Hispaniola (Fig. 10).

There are places where probabilities derived from the empirical rate observations are higher than the numerical models predict. In particular this is seen at Puerto Rico, Jamaica, Costa Rica, and Panama. In these instances it is likely that the empirical model has captured localized tsunami events that were caused by landslides and/or accommodating faults associated with the plate boundary that were not specifically included in the numerical model sources. Many of the secondary earthquake sources not included have very slow and uncertain slip rates, making implementation into a numerical model difficult.

10. Combination of Empirical and Modeled tsunami Runup Rates through a Bayesian Process with Likelihood Functions

As with any probabilistic forecast, we were confronted with considerable uncertainty from many sources. Key sources of epistemic uncertainty included: (1) Expected tsunami runup rates, (2) tsunami sources not explicitly known or included in the model, (3) seismic coupling coefficient of the Caribbean plate boundary zones, and (4) degree of completeness in the empirical tsunami catalog. To encompass these uncertainties into our probability estimates, we created a Bayesian framework to build tsunami runup rate estimates within 20 km by 20 km cells that contain coastlines throughout the Caribbean region. The key advantage of our approach is that the model results end up being weighted by their attendant uncertainties.

We combined model and empirical rates which addressed the above-listed uncertainties as follows. (1) Runup-rate uncertainty: Monte Carlo rate-model fits to the

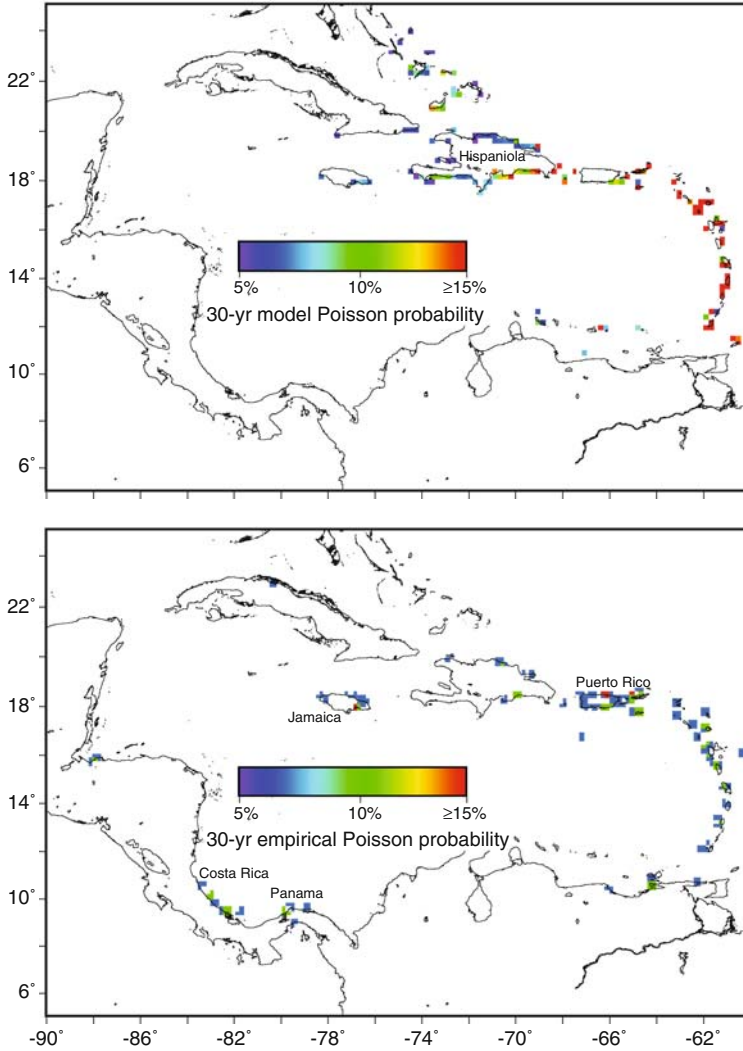


Figure 10

Comparison between (top) model-derived 30-year Poisson probability of tsunami runups (≥ 0.5 m) and (bottom) empirically derived values. See text for discussion.

empirical rates as shown in Figure 3 along with results from 50 numerical model runs provided arrays of possible runup rate values at each cell. (2) Unknown/unaccounted-for tsunami sources: Inclusion of the empirical rates added sources not accounted for in the numerical model (most-affected areas can be seen by comparing the panels of Fig. 10); our forecast may suffer from incomplete knowledge if events not covered by our numerical models have also not occurred in the empirical catalog over the past 500 years.

(3) Seismic coupling: The empirical model implies low seismic coupling of 0.32, whereas the numerical models have coupling coefficients of 1.0. (4) Completeness: We accounted for low-rate plate-boundary events potentially not seen in the empirical catalog with the 50 numerical model runs.

As described in more detail below, we combined our model-derived runup rates with empirical rates according to the following set of logic-tree branches: In cells where there were no empirical values, the numerical model-derived rates were given full weight. Conversely, empirical rates were given full weight where numerical model rates were zero. Lastly, where there were empirical and model rate estimates within the same cells, we used Bayesian likelihood functions to weight the two models. Distributions shown in Figure 3 give the relative probability of different rates for a Poisson model that could have caused the empirical observations. Similarly, results from the 50 numerical model runs produced relative probability (Fig. 11) of different rates in each model cell.

To rank different rate models for each cell where more than one estimate existed, we made a likelihood calculation to weight the models. In the simplest binomial case likelihood is defined as proportional to the probability of obtaining results A given a fixed hypothesis H resulting from a set of fixed data. If A_1 and A_2 are two possible mutually exclusive results, then

$$P(A_1 \text{ or } A_2|H) = P(A_1|H) + P(A_2|H), \quad (9)$$

and likelihood is thus

$$L(H|A) = kP(A|H), \quad (10)$$

where k is an arbitrary constant.

The results from likelihood functions were used to obtain the final weights using Bayes' rule (Equation (11)), where the posterior distribution is proportional to the likelihood function multiplied by the prior. For our study, we used a uniform (noninformative) prior such that there was equal probability of all rates in each coastal 20 km by 20 km cell. Further, since we update the prior twice, once for the empirical result, and again for the numerical result, the same result is achieved by simply multiplying the two likelihood functions. Thus the likelihood of a given rate λ where there were empirical estimates ($e1$) and numerical-modeled estimates ($e2$) is

$$L(\lambda|e1, e2) = k[p_1(e1|\lambda)][p_2(e2|\lambda)], \quad (11)$$

where $p(e1|\lambda)$ is the probability of rate λ based on the Monte Carlo fits shown in Figure 3, and $p(e2|\lambda)$ is the probability of rate λ from the 50 numerical model runs. The constant k is used for normalizing the weights so that they add to 1.

We used likelihood functions to weight rate models over a range from 0 to 10 events in the 500-yr observation period. We considered rates between 0 and 10 events in 500 years for all cells, assuming no further prior information. Final rates were found by weighted means of the posterior rates. To summarize the process, where model and

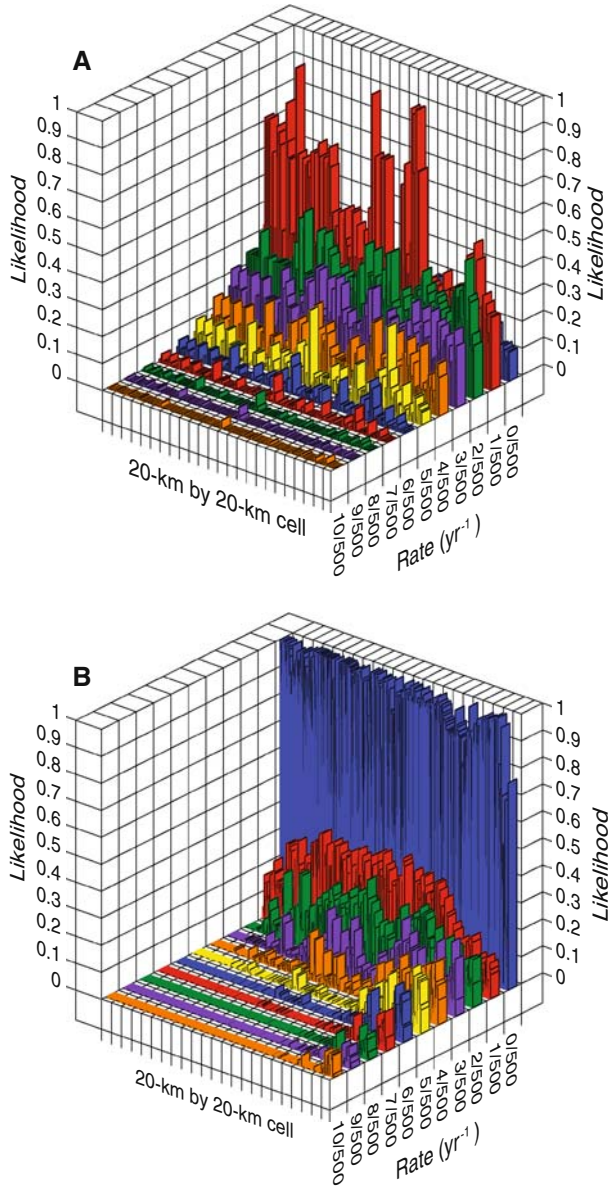


Figure 11

(a) Normalized histogram (likelihood) of tsunami runup ($R_0 \geq 0.5$ m) rates in 214 20-km by 20-km cells defined using likelihood functions from empirical rates (Fig. 3) and from 50 numerical modeling simulations. (b) Normalized histogram of runup rates from numerical modeling in 685 cells where there were no empirical observations. Mean values from these distributions were used in the best-estimate probability calculations mapped in Figure 12.

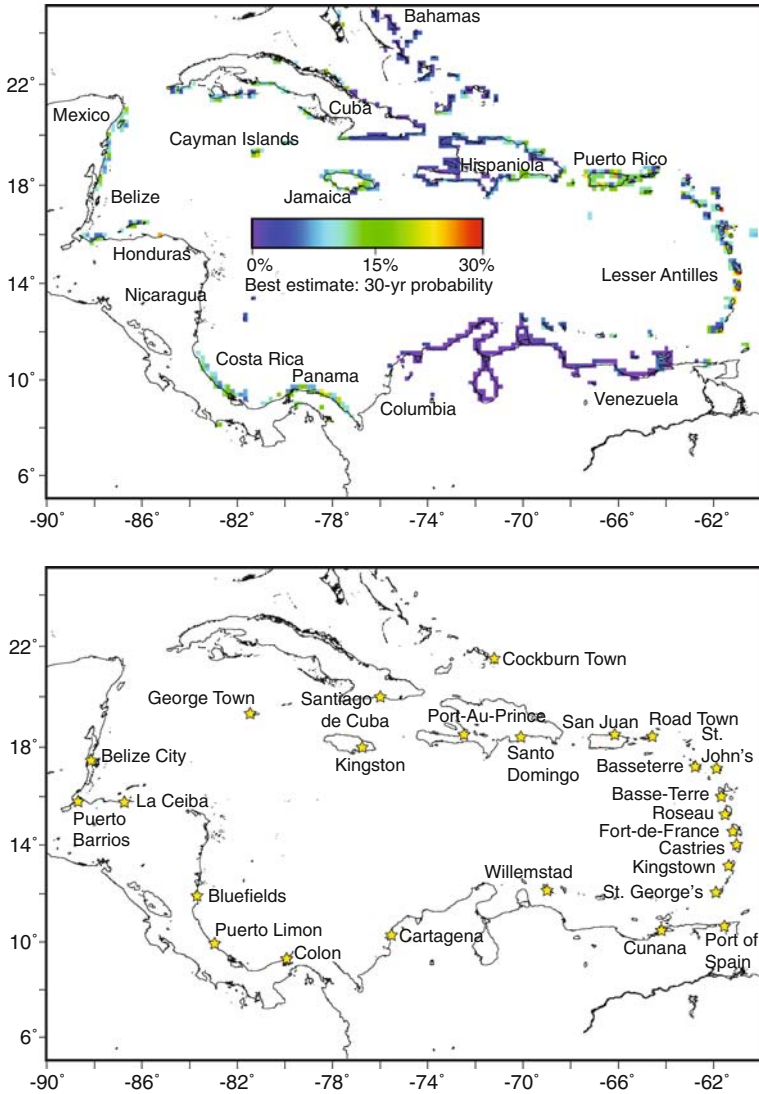


Figure 12

30-year tsunami runup ($r \geq 0.5$ m) probability in 20 km by 20 km cells at coastal sites in the Caribbean region made from combined rate estimates from empirical and numerical models. Lower panel shows locations of cities listed in Table 3.

empirical values were both absent for a given rate, the posterior distribution was zeroed. When one model provided rates, its likelihood function was used to update the priors, and when both empirical and numerical rate estimates were available, likelihood was developed through combination and renormalization using Equation (11), which was then used to update the priors.

Table 3

30-year probability of tsunami runup in excess of 0.5 m in cells that contain population concentrations in 20 km by 20 km cells for representative Caribbean countries and territories. Population given as a relative measure of risk throughout the region. Values were calculated as uniform over cell areas, and are not intended to convey any detail at selected cities, but are presented for comparison purposes. Dashes indicate negligible calculated probability.

Country	Nearest coastal city in 20 km × 20 km cell	Latitude	Longitude	Population	30-yr probability $r \geq 0.5$ m (%)
Antigua and Barbuda	St. John's	17.1167°	-61.8500°	24,226	5.74
Belize	Belize City	17.4847°	-88.1833°	70,800	-
Cayman Islands	George Town	19.3034°	-81.3863°	20,626	10.79
Columbia	Cartagena	10.4000°	-75.5000°	895,400	0.08
Costa Rica	Puerto Limon	10.000°	-83.0300°	78,909	8.32
Cuba	Santiago de Cuba	20.0198°	-75.8139°	494,337	2.31
Dominica	Roseau	15.3000°	-61.3833°	14,847	11.94
Dominican Republic	Santo Domingo	18.5000°	-69.9833°	913,540	17.56
France, Guadeloupe	Basse-Terre	16.2480°	-61.5430°	44,864	11.79
France, Martinique	Fort-de-France	14.5833°	-61.0667°	94,049	5.33
Grenada	St. George's	12.0500°	-61.7500°	7,500	2.48
Guatemala	Puerto Barrios	15.7308°	-88.5833°	40,900	-
Haiti	Port-Au-Prince	18.5333°	-72.3333°	1,277,000	0.01
Honduras	La Ceiba	15.7667°	-86.8333°	250,000	-
Jamaica	Kingston	17.9833°	-76.8000°	660,000	21.95
Netherlands Antilles	Willemstad	12.1167°	-68.9333°	125,000	7.04
Nicaragua	Bluefields	12.0000°	-83.7500°	45,547	-
Panama	Colon	9.3333°	-79.9000°	204,000	17.56
St. Kitts and Nevis	Basseterre	17.3000°	-62.7333°	15,500	6.95
St. Lucia	Castries	14.0167°	-60.9833°	10,634	5.52
St. Vincent and the Grenadines	Kingstown	13.1667°	-61.2333°	25,307	11.32
Trinidad and Tobago	Port of Spain	10.6667°	-61.5167°	49,031	-
Turks and Caicos	Cockburn Town	21.4590°	-71.1390°	5,567	3.57
UK, Virgin Islands	Road Town	18.4333°	-64.5000°	9,400	13.85
USA, Puerto Rico	San Juan	18.4500°	-66.0667°	434,374	22.24
USA, Virgin Islands	Charlotte Amalie	18.3500°	-64.9500°	18,914	17.56
Venezuela	Cunana	10.4564°	-64.1675°	305,000	6.27

11. Probability Results from the Rate Model

We calculated a best-estimate set of 30-year tsunami runup probability ($R_0 \geq 0.5$ m) values for the 20 km by 20 km coastal cells throughout the Caribbean region (Fig. 12). Generally, the highest probabilities (typically 10–20% in 30 years for runup $R_0 \geq 0.5$ m) we calculated were for the eastern Lesser Antilles, including the Islands of Antigua, Barbuda, Dominica, Guadeloupe, Martinique, Grenada, St. Kitts, Nevis, St. Lucia, St. Vincent, and the Grenadines (Fig. 12, Table 3). Additionally, relatively higher hazard was calculated for the easternmost Greater Antilles including the Virgin Islands, Puerto Rico, and eastern Hispaniola. These sites were elevated primarily because of their proximity to the Caribbean-North American subduction plate boundary. However, we

also forecasted relatively high hazard from the Cayman transform boundary at Jamaica, driven primarily by empirical rate estimates. The empirical rate model also significantly effected for Costa Rica and Panama, likely caused by events along the north Panama convergence zone in addition to basin-wide tsunamis, for which we calculated relatively high probabilities (Fig. 12).

For reference, we give the calculated 30-year probability of tsunami runup ($r \geq 0.5$ m) in cells that contain population concentrations in 20 km by 20 km cells for representative Caribbean countries and territories in Table 3. Probabilities do not take into account the relative vulnerability of the populations at different sites related to specifics of coastal topography and very near-shore bathymetry. Thus maps and tables presented here might best be applied as sources of relative hazard, subject to corrections related to local site variations

12. Conclusions

Combination of a ~ 500 -year period of tsunami runup observations with numerical modeling enabled us to make a coarsely-sampled (20 km by 20 km) tsunami hazard map of the Caribbean region. The primary source of uncertainty is the degree of completeness that a 500-year catalog represents. We found that we cannot quantify this uncertainty without knowledge of the seismic coupling coefficient of the Caribbean-North American plate boundary zones. We thus used likelihood functions to weight an empirical tsunami runup rate estimate that suggested a very low seismic coupling coefficient of $c = 0.32$ against numerical models of tsunami runup that assumed full coupling ($c = 1$). Combining empirical and modeled rates made up for some of the deficiencies in each approach; the empirical catalog is likely not a complete record of all possible interplate tsunami sources, whereas the numerical model did not account for accommodating intra-plate faults and/or landslide sources that appear likely causes of tsunamis in the empirical record.

REFERENCES

- AIDA, I. (1969), *Numerical experiments for the tsunami propagation—The 1964 Niigata tsunami and the 1968 Tokachi-Oki tsunami*, Bull. Earthq. Res. Insti. 47, 673–700.
- AUDEMARD, F. E. and AUDEMARD, F. A. (2002), *Structure of the Mérida Andes, Venezuela: Relations with the South America-Caribbean geodynamic interaction*, Tectonophysics 345, 299–327.
- BIRD, P. and KAGAN, Y. Y. (2004), *Plate-tectonic analysis of shallow seismicity: Apparent boundary width, beta-value, corner magnitude, coupled lithosphere thickness, and coupling in 7 tectonic settings*, Bull. Seismol. Soc. Am. 94, 2380–2399.
- CATTIN, R., LYON-CAEN, H., and CHÉRY, J. (1997), *Quantification of interplate coupling in subduction zones and forearc topography*, Geophys. Res. Lett. 24, 1563–1566.
- CRUCIANI, C., CARMINATI, E., and DOGLIONI, C. (2005), *Slab dip vs. lithosphere age: No direct function*, Earth Planet. Sci. Lett. 238, 298–310.

- DEMETTS, C., JANSMA, P. E., MATTIOLI, G. S., DIXON, T. H., FARINA, F., BILHAM, R., CALAIS, E., and MANN, P. (2000), *GPS geodetic constraints on Caribbean-North American plate motion*, *Geophys. Res. Lett.* 27, 437–440.
- DIXON, T. H., FARINA, F., DEMETTS, C., JANSMA, P., MANN, P., and CALAIS, E. (1998), *Relative motion between the Caribbean and North American plates and related boundary zone deformation from a decade of GPS observations*, *J. Geophys. Res.* 103, 15157–15182.
- GEIST, E. L. (2002), *Complex earthquake rupture and local tsunamis*, *J. Geophys. Res.* 107, doi:10.1029/2000JB000139.
- GEIST, E. L. and PARSONS, T. (2006), *Probabilistic analysis of tsunami hazards*, *Natural Hazards* 37, 277–314.
- GEIST, E. L. and PARSONS, T. (2008), *Distribution of tsunami inter-event times*, *Geophys. Res. Lett.* 35, doi:10.1029/2007GL032690.
- GEIST, E. L., PARSONS, T., IEN BRINK, U. S., and LEE, H. J., *Tsunami Probability*. In *The Sea* (eds. Bernard, E. N. and Robinson, A. R.) (Harvard University Press, Cambridge, Massachusetts (2008)), in press.
- GELLER, R. J. (1976), *Scaling relations for earthquake source parameters and magnitudes*, *Bull. Seismol. Soc. Am.* 66, 1501–1523.
- GRINDLAY, N. R., HEARNE, M., and MANN, P. (2005), *High risk of tsunami in the northern Caribbean*, *EOS Trans.* 86, 121–132.
- HANKS, T. C. and KANAMORI, H. (1979), *A moment magnitude scale*, *J. Geophys. Res.* 84, 2348–2350.
- HERRERO, A. and BERNARD, P. (1994), *A kinematic self-similar rupture process for earthquakes*, *Bull. Seismol. Soc. Am.* 84, 1216–1228.
- KAGAN, Y. Y. (2002a), *Seismic moment distribution revisited: I, Statistical Results*, *Geophys. J. Int.* 148, 520–541.
- KAGAN, Y. Y. (2002b), *Seismic moment distribution revisited: II, Moment conservation principle*, *Geophys. J. Int.* 149, 731–754.
- KAGAN, Y. Y. and JACKSON, D. D. (2000), *Probabilistic forecasting of earthquakes*, *Geophys. J. Int.* 143, 438–453.
- KOPF A., and BROWN, K. M. (2003), *Friction experiments on saturated sediments and their implications for the stress state of the Nankai and Barbados subduction thrusts*, *Marine Geology* 202, 193–210.
- LAY, T., KANAMORI, H., and RUFF, L. J. (1982), *The asperity model and the nature of large subduction zone earthquakes*, *Earthq. Predict. Res.* 1, 3–71.
- LEROY, S., MAUFFRET, A., PATRIAT, P., and MERCIER DE LÉPINAY, B. (2000), *An alternative interpretation of the Cayman trough evolution from a reidentification of magnetic anomalies*, *Geophys. J. Int.* 141, 539–557.
- MANN, P., ROGERS, R., and GAHAGAN, L., *Overview of plate tectonic history and its unresolved tectonic problems*. In *Central America: Geology, Resources, and Hazards* vol. 1 (eds. Bundschuh, J. and Alvarado, G.) (Taylor and Francis/Balkema, Leiden, The Netherlands 2007), pp. 201–237.
- MATSUYAMA, M., WALSH, J. P., and YEH, H. (1999), *The effect of bathymetry on tsunami characteristics at Sissano Lagoon, Papua New Guinea*, *Geophys. Res. Lett.* 26, 3513–3516.
- MCCAFFREY, R. (1994), *Dependence of earthquake size distributions on convergence rates at subduction zones*, *Geophys. Res. Lett.* 21, 2327–2330.
- OKADA, Y. (1985), *Surface deformation due to shear and tensile faults in a half-space*, *Bull. Seismol. Soc. Am.* 75, 1135–1154.
- O'LOUGHLIN, K. F. and LANDER, J. F., *Caribbean Tsunamis: A 500-Year History from 1498–1998* (Kluwer Academic Publishers, Dordrecht, The Netherlands (2003)).
- PARSONS, T. (2008), *Monte Carlo method for determining earthquake recurrence parameters from short paleoseismic catalogs: Example calculations for California*, *J. Geophys. Res.* 112, doi:10.1029/2007JB004998.
- REID, R. O. and BODINE, B. R. (1968), *Numerical model for storm surges in Galveston Bay*, *J. Waterways and Harbors Div., A.C.E.* 94, 33–57.
- RUFF, L. J., *State of stress within the Earth*. In *International Handbook of Earthquake and Engineering Seismology*, 81A (eds. Lee, W. H. K., Kanamori, H., Jennings, P. C., and Kisslinger, C.) (Academic Press, Amsterdam 2002) pp. 539–557.
- SATAKE, K. (1995), *Linear and nonlinear computations of the 1992 Nicaragua earthquake tsunami*, *Pure Appl. Geophys.*, 144, 455–470.

- SATAKE, K., *Tsunamis*. In *International Handbook of Earthquake and Engineering Seismology*, 81A (eds. Lee, W. H. K., Kanimori, H., Jennings, P. C., and Kisslinger, C.) (Academic Press, Amsterdam 2002) pp. 437–451.
- SHEPHERD, J.B., *Seismic hazard in the eastern Caribbean*. In *The Practice of Earthquake Hazard Assessment* (ed. McGuire, R.K.) (IASPEI, Denver (1993)) pp. 51–55.
- SHUTO, N. (1991), *Numerical simulation of tsunamis—Its present and near future*, *Natural Hazards* 4, 171–191.
- SMITH, W. H. F. and SANDWELL, D. T. (1997), *Global seafloor topography from satellite altimetry and ship depth soundings*, *Science* 277, 1957–1962.
- TANIOKA, Y. and SATAKE, K. (1996), *Tsunami generation by horizontal displacement of ocean bottom*, *Geophys. Res. Lett.* 23, 861–865.
- TEN BRINK, U. S. and LIN, J. (2004), *Stress interaction between subduction earthquakes and forearc strike-slip faults: Modeling and application to the northern Caribbean plate boundary*, *J. Geophys. Res.* 109, doi:12310.11029/12004JB003031.
- TITOV, V. V. and SYNOLAKIS, C. E. (1997), *Extreme inundation flows during the Hokkaido-Nansei-Oki tsunami*, *Geophys. Res. Lett.* 24, 1315–1318.
- TSAI, C. P. (1997), *Slip, stress drop and ground motion of earthquakes: A view from the perspective of fractional Brownian motion*, *Pure Appli. Geophys.* 149, 689–706.
- WELLS, D. L., and COPPERSMITH, K. J. (1994), *New empirical relationships among magnitude, rupture length, rupture width, rupture area, and surface displacement*, *Bull. Seismol. Soc. Am.* 84, 974–1002.

(Received December 12, 2007, revised August 19, 2008)

Published Online First: December 19, 2008

To access this journal online:
www.birkhauser.ch/pageoph
